SUPPLEMENTARY INFORMATION

For "High reliability Ag@Ni-NiO Nanowire-Based SERS for cancer detection: A study on breast cancer"

Alondra Hernandez Cedillo, *[a,b] J. Mendez-Lozoya [a,b], Coral Hernandez Cedillo, [a,b] Alfred L. M. Bothwell, [c,d] and Miguel Jose Yacaman [a,b]

[a] Department of Applied Physics and Materials Science, Northern Arizona University, Flagstaff, Arizona, 86011, USA

[b] Center for Materials Interfaces in Research and Applications, Northern Arizona University, Flagstaff, Arizona 86011, USA

[c] Department of Pathology, Microbiology, and Immunology, University of Nebraska Medical Center, Omaha, Nebraska, 68198, USA

[d] Department of Immunobiology, Yale University School of Medicine, New Haven, Connecticut, 06520, USA

* Corresponding author: ah3526@nau.edu

Contents

Fig. S1. presents how de-waxing was performed using sequential ethanol, hexane, and water washes prior to SERS acquisition. The spectra exhibit highly similar peak positions and relative intensities across the measured range, indicating that paraffin removal does not significantly alter the observed Raman signatures under the conditions used in this study.

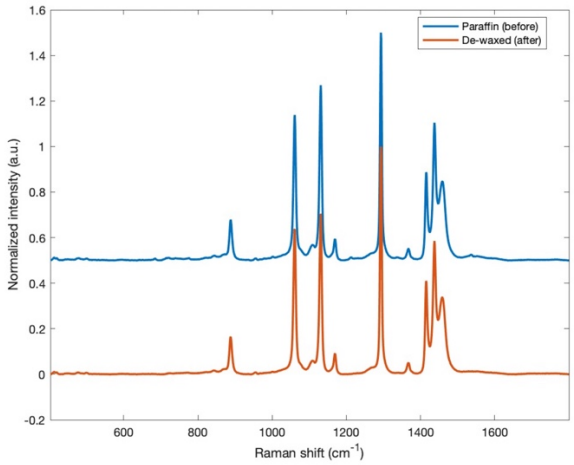

Fig. S1 Comparison of SERS spectra obtained from FFPE breast tissue sections before and after deparaffinization.

Table S1 provides a comprehensive list of SERS peaks (400-1700 cm^{-1}), together with their corresponding vibrational assignments and supporting literature references. This table serves as the reference framework for interpreting the spectral features discussed in the subtype-specific tables that follow.

Table S1 Complete Surface-Enhanced Raman Scattering (SERS) peaks and vibrational mode assignments.

SERS shift (cm^{-1})	Assignment	Reference
420	D-(-)-Fructose, citric acid	(56)
436	β − D-glucose	(56)
446	Lactose, glutathione	(56)
482	Saccharides, glycogen	(59,66)
534	S-S disulphide bridges in cysteine	(67)
563	Tryptophan/cytosine, guanine	(59)
599	Glycerol, Tryptophan, phosphatidylinositol	(66)
609	C-C twisting thymine	(54,66)
645	C-C twisting tyrosine, C-S stretching	(49,54)
671	C–S stretching mode of cystine, guanine, thymine, phospholipids in nucleic acids	(59,66,68)

684	Succinic acid	(56)
707	Adenine	(54)
722	$N^+(CH_3)3$, choline group, stretch band, C-N (membrane phospholipid head)/nucleotide peak, characteristic for phosphatidylcholine, sphingomyelin	(49)
731	$N^+(CH_3)_3$ symmetric stretching of phosphatidylcholine lipids	(59)
750	Proteins, symmetric ring breathing in tryptophan	(66,68)
775	Ring breathing mode of pyrimidine	(54)
807	O−P−O stretch (DNA), tyrosine, ring breathing mode of uracil	(54,59,69)
817	C—C stretch of proline and hydroxyproline, out of plane ring breathing of tyrosine assigned to CH_2 twisting of lipids in healthy	(70)
846	C-O-C skeletal mode, monosaccharides, tyrosine, single bond stretching vibrations for amino acids	(49,54,66)
869	C-C stretching, collagen, lipid, hydroxyproline (collagen I), Saccharides, proline, saccharides	(49,55,66,68)
876	ρ(CH2) protein	(55)
892	Structure protein modes of tumors	(49)
935	C-C protein backbone α-helix(proline/glycogen), collagen, skeletal C-C, α-helix, ν(C-C), valine	(49,54,57,67)
965	Lipids, δ(= CH) wagging, stretching C-O ribose	(49,54,66)
1005	Phenylalanine (collagen), ν(C-C) symmetric ring breathing mode	(48,55,57,67-69,71)
1026	C−H in-plane bending mode of phenylalanine	(57,59)
1041	Collagen	(49)
1065	Chain C-C stretch in lipids; C-O and C-N stretch in proteins; O-P-O stretch in DNA and RNA, proline (collagen)	(48,49)
1092	C-C stretch, phospholipids O-P-O	(54,55,66)
1112	C-C stretch (lipid), saccharides	(49,54,55)
1135	C-C skeletal stretching	(54)
1173	C-H bending tyrosine	(49)
1179	Phenylalanine, tryptophan, tyrosine	(57,59)
1221	Amide III	(59)
1236	β-sheet, amide III, CH_2 wagging of glycine and proline	(66)
1244	Amide III	(54,71)

1268	Amide III (α-helix), collagen, lipids	(48,68,69)
1297	Cytosine, ν(CN) and ν(NH) modes of the peptide bond ν(-CONH)	(54,57)
1339	CH_2 deformation lipid/adenine, cytosine, tryptophan, α-helix, phospholipids	(59,66)
1371	δCH_3 symmetric lipid	(55)
1419	Deoxyribose	(54)
1441	CH_2 bending mode in lipids, cholesterol, fatty acid, C–O symmetric stretching	(48,49,55,59,66,71)
1463	Stearic acid	(56)
1531	Adenine, guanine, cytosine	(66)
1556	C=C stretching in tryptophan	(68)
1599	C=C bending mode of phenylalanine, tyrosine, C=C olefinic stretch, ν(C = C) modes of aromatic amino acids	(54,57,59,69)
1611	C=C stretching in phenylalanine, tyrosine, and tryptophan)	(57,68)
1656	C=C lipid stretching, ν(C=O), α-helix (Amide I)	(49,67,68,71)
1692	C=O stretch lipid	(59)

Triple-Negative Breast Cancer

Table S2 summarizes the distribution of SERS spectral shifts consistently observed in the Triple-Negative Breast Cancer (TNBC) subtype. Characteristic peaks include 892, 1065, 1112, 1135, 1297, 1371, 1419, 1441, and 1463 cm^{-1}, which were recurrent across TNBC samples. The 892 cm^{-1} band is attributed to protein structural vibrations (49). The 1065 cm^{-1} peak corresponds primarily to C-C stretching in lipids and has also been associated with C-O and C-N stretching in proteins, O-P-O vibrations of DNA and RNA, and the amino acid proline, which is abundant in collagen (48,49,59). The 1112 cm^{-1} band is indicative of C-C stretching in polysaccharides (54,55,59), while the 1135 cm^{-1} peak corresponds to C-C skeletal vibrations (54). The 1297 cm^{-1} band is assigned to cytosine and ν(CN) and ν(NH) vibrations of peptide bonds (-CONH) (54,57).

Additional TNBC-associated peaks include 1317 cm^{-1}, attributed to CH_2 deformation in lipids and contributions from adenine, cytosine, tryptophan, α-helical protein structures, and phospholipids (59,66); 1419 cm^{-1}, corresponding to deoxyribose vibrations (54); 1441 cm^{-1}, associated with CH_2 bending modes in lipids, cholesterol, and fatty acids (48,49,55,59,66,71); and 1463 cm^{-1}, assigned to stearic acid (56). TNBC-associated peaks are highlighted in bold in Table S2

Surface-Enhanced Raman Scattering (SERS) analysis of TNBC subtypes (TNBC1-TNBC8) revealed distinct molecular fingerprints involving carbohydrates, nucleic acids, proteins, and lipids. Carbohydrate-related peaks at 420, 482, and 869 cm^{-1} were

frequently observed, indicating altered sugar metabolism and glycosylation patterns. Nucleic-acid-associated signals at 563, 671, and 731 cm^{-1} highlight contributions from DNA/RNA bases and phospholipid headgroups. Protein-related bands at 892, 1005, 1173, 1297, and 1556 cm^{-1} were dominant, reflecting protein backbone vibrations, aromatic amino acid contributions, and changes in secondary structure. Lipid-associated peaks at 1065, 1112, 1371, 1441, 1463, and 1692 cm^{-1} consistently reflected disruptions in membrane composition, fatty-acid content, and cholesterol metabolism.

Collectively, these spectral features illustrate the pronounced biochemical heterogeneity of TNBC subtypes and underscore the utility of SERS as a sensitive analytical tool for distinguishing molecular phenotypes in triple-negative breast cancer.

Table S2 Distribution of SERS shifts in Triple-Negative Breast Cancer (TNBC) Subtype.

SERS shift (cm^{-1})	**TNBC 1**	**TNBC 2**	**TNBC 3**	**TNBC 4**	**TNBC 5**	**TNBC 6**	**TNBC 7**	**TNBC 8**	**Assignment**
420	x	x	x	x	x		x	x	D-(-)-Fructose, citric acid
436	x								β-D-glucose
446						x			Lactose, glutathione
482	x		x		x	x	x	x	Saccharides, glycogen
534		x	x						S-S disulphide bridges in cysteine
563	x	x							Tryptophan / cytosine, guanine
599						x			Glycerol, tryptophan, phosphatidylinositol
609		x							C-C twisting, thymine
671	x		x					x	C-S stretching of cystine; guanine, thymine; phospholipids in nucleic acids
684						x			Succinic acid
707				x	x				Adenine
722						x	x		$N^{+}(CH_3)_3$ choline group; phosphatidylcholine, sphingomyelin; membrane phospholipid headgroup
731	x	x	x	x				x	$N^{+}(CH_3)_3$ symmetric stretching of phosphatidylcholine lipids
750						x			Proteins; symmetric ring breathing of tryptophan
775	x	x		x					Ring breathing mode of pyrimidine
807	x				x				O-P-O stretch (DNA); tyrosine; uracil ring breathing
817		x							C-C stretch of proline/hydroxyproline; tyrosine ring breathing; CH_2 twisting of lipids
846				x					C-O-C skeletal mode; monosaccharides; tyrosine; amino acid single-bond stretching
869	x	x						x	C-C stretching; collagen; lipids; hydroxyproline (collagen I); saccharides, proline
876			x	x		x	x		$\rho(CH_2)$ protein
892	**x**	**x**	**x**	**x**	**x**	**x**	**x**	**x**	Protein structural modes (tumor-related)
935	x	x				x			C-C protein backbone (α-helix); proline/glycogen; collagen; valine
965	x			x	x	x	x		Lipids; δ(=CH) wagging; C-O stretching of ribose
1005	x	x	x		x		x	x	Phenylalanine; symmetric ring breathing; collagen

1041							x	x	Collagen
1065	**x**	**x**	**x**	**x**	**x**	**x**	**x**	**x**	C-C stretch in lipids; C-O and C-N stretch in proteins; O-P-O (DNA/RNA); proline (collagen)
1112	**x**	**x**	**x**	**x**	**x**	**x**	**x**	**x**	C-C stretch (lipids); saccharides
1135	**x**	**x**	**x**	**x**	**x**	**x**	**x**	**x**	C-C skeletal stretching
1173	x	x	x	x	x	x			C-H bending of tyrosine
1179					x		x	x	Phenylalanine, tryptophan, tyrosine
1221						x			Amide III
1236	x	x	x		x		x	x	β-sheet; Amide III; CH_2 wagging of glycine and proline
1268		x	x	x		x			Amide III (α-helix); collagen; lipids
1297	**x**	**x**	**x**	**x**	**x**	**x**	**x**	**x**	Cytosine; v(CN) and v(NH); peptide bond (-CONH)
1339	x	x	x			x			CH_2 deformation (lipids); adenine, cytosine, tryptophan; α-helix; phospholipids
1371	**x**	**x**	**x**	**x**	**x**	**x**	**x**	**x**	$\delta(CH_3)$ symmetric lipid
1419	**x**	**x**	**x**	**x**	**x**	**x**	**x**	**x**	Deoxyribose
1441	**x**	**x**	**x**	**x**	**x**	**x**	**x**	**x**	CH_2 bending (lipids); cholesterol; fatty acids; C-O symmetric stretching
1463	**x**	**x**	**x**	**x**	**x**	**x**	**x**	**x**	Stearic acid
1531						x			Adenine, guanine, cytosine
1556	x	x		x	x	x	x	x	C=C stretching in tryptophan
1599				x					C=C bending of phenylalanine, tyrosine; aromatic amino acids
1611						x	x		C=C stretching in phenylalanine, tyrosine, tryptophan
1656			x						Amide I (α-helix); C=O stretching; lipid C=C
1692	x	x					x	x	C=O stretching in lipids

HER2-enriched

In contrast to TNBC, **Table S3** summarizes the distribution of SERS spectral shifts observed in the HER2-enriched breast cancer subtype. Prominent peaks were detected at 1062, 1133, 1171, 1295, 1369, 1417, 1438, and 1461 cm^{-1}. The 1062 cm^{-1} band is primarily attributed to C-C stretching in lipids and also includes contributions from C-O and C-N stretching in proteins and phosphate vibrations in nucleic acids (48,49). The 1133 cm^{-1} peak corresponds to C-C skeletal stretching (54), while the 1171 cm^{-1} band is assigned to C-H bending modes of tyrosine residues (49). The 1295 cm^{-1} peak is associated with cytosine and v(CN) and v(NH) vibrations of peptide bonds (54,57).

Additional lipid-related features include 1369 cm^{-1}, corresponding to symmetric CH_3 deformation in lipids (55), 1417 cm^{-1}, attributed to deoxyribose vibrations (54), 1438 cm^{-1}, associated with CH_2 bending modes in lipids and fatty acids, and 1461 cm^{-1}, assigned to stearic acid (56).

Notably, the 892 cm^{-1} band (protein structural vibrations) and the 1112 cm^{-1} band (C-C stretching in polysaccharides), which are consistently observed in TNBC samples, are absent in the HER2-enriched subtype. The lack of these peaks may reflect HER2-driven alterations in protein organization and reduced polysaccharide contributions, potentially associated with membrane-dominated signaling and receptor overexpression.

Surface-Enhanced Raman Scattering (SERS) analysis of HER2-enriched breast cancer samples (HER2_2-HER2_5) revealed a consistent biochemical fingerprint involving carbohydrates, lipids, proteins, and nucleic acids. Carbohydrate-related peaks at 418 and 482 cm^{-1} indicate altered sugar metabolism. Strong membrane lipid signals at 720-731, 1062, 1111, 1133, and 1660-1686 cm^{-1} highlight phospholipid remodeling and membrane reorganization, which are hallmarks of HER2-positive tumor aggressiveness. Protein-associated bands at 817, 873, 889, 1002, 1171, 1268, and 1295 cm^{-1} reflect amino acid contributions, protein backbone vibrations, and changes in secondary structure. Nucleic-acid-associated features at 525, 662, and 1369-1461 cm^{-1} suggest increased genomic activity and replication demands.

Collectively, these spectral characteristics reflect metabolic reprogramming, membrane phospholipid enrichment, and protein-lipid structural interplay in HER2-enriched tumors, underscoring the aggressive biological behavior of this breast cancer subtype and the sensitivity of SERS in capturing subtype-specific molecular signatures.

Table S3 Distribution of SERS shifts in HER2-enriched Subtype.

SERS shift (cm^{-1})	**HER2_ 2**	**HER2_ 3**	**HER2_ 4**	**HER2_ 5**	**Assignment**
418	x	x		x	D-(-)-Fructose, citric acid
482			x		Saccharides, glycogen
525			x		S-S disulphide bridges in cysteine
662			x		C-S stretching of cystine; guanine, thymine; phospholipids in nucleic acids
720	x	x		x	$N^+(CH_3)_3$ choline group; phosphatidylcholine, sphingomyelin (membrane phospholipid headgroup)
751			x		Proteins; symmetric ring breathing of tryptophan
817	x	x		x	C-C stretch of proline/hydroxyproline; tyrosine ring breathing; CH_2 twisting of lipids
873	x	x			C-O-C skeletal mode; monosaccharides; tyrosine; amino acid single-bond stretching
848	x			x	C-C stretching; collagen; lipids; hydroxyproline (collagen I); saccharides, proline
866			x	x	Protein structural modes (tumor-related)
889	x	x		x	C-C protein backbone (α-helix); collagen; proline/glycogen
935			x		Lipids; δ(=CH) wagging; C-O stretching of ribose
956				x	Phenylalanine; symmetric ring breathing; collagen
1002	x	x			C-H in-plane bending of phenylalanine / collagen contribution
1111				x	C-C stretch in lipids; C-O/C-N stretch in proteins; O-P-O (DNA/RNA); proline (collagen)
1033	x		x		C-C stretch; phospholipid O-P-O
1062	**x**	**x**	**x**	**x**	C-C stretch (lipids); saccharides
1092			x		C-C skeletal stretching
1107	x				C-H bending of tyrosine
1133	**x**	**x**	**x**	**x**	Amide III
1171	**x**	**x**	**x**	**x**	β-sheet; Amide III; CH_2 wagging of glycine and proline
1215			x		Amide III (α-helix); collagen; lipids
1236	x				Cytosine; v(CN) and v(NH); peptide bond (-CONH)
1268	x	x	x		$\delta(CH_3)$ symmetric lipid
1295	**x**	**x**	**x**	**x**	Deoxyribose
1369	**x**	**x**	**x**	**x**	CH_2 bending (lipids); cholesterol; fatty acids; C-O symmetric stretching
1417	**x**	**x**	**x**	**x**	Stearic acid
1438	**x**	**x**	**x**	**x**	Amide I (α-helix); C=O stretching; lipid C=C
1461	**x**	**x**	**x**	**x**	C=O stretching in lipids

1660			x		
1686	x				

Luminal A

Table S4 outlines the distribution of SERS spectral shifts observed in the Luminal A (LUMA) breast cancer subtype. Recurrent peaks were detected at 892, 1064, 1112, 1135, 1172, 1297, 1370, 1418, and 1440 cm^{-1}.The 892 cm^{-1} band is attributed to protein structural vibrations (49). The 1064 cm^{-1} peak corresponds primarily to C-C stretching in lipids and also includes contributions from C-O and C-N stretching in proteins and phosphate vibrations in nucleic acids (48,49). The 1112 cm^{-1} band is assigned to C-C stretching in lipids and saccharides (49,54,55), while the 1135 cm^{-1} peak corresponds to C-C skeletal vibrations (54). The 1172 cm^{-1} band is associated with C-H bending modes of tyrosine residues (49), and the 1297 cm^{-1} peak is attributed to cytosine and ν(CN) and ν(NH) vibrations of peptide bonds (-CONH) (54,57). Lipid-associated bands at 1370 cm^{-1}, 1418 cm^{-1}, and 1440 cm^{-1} correspond to symmetric CH_3 deformation, deoxyribose vibrations, and CH_2 bending modes in lipids and fatty acids, respectively (2-3, 6, 10, 13-14, 55).

Unlike TNBC and HER2-enriched subtypes, Luminal A samples consistently exhibit a pronounced 1112 cm^{-1} feature, reflecting combined lipid and saccharide contributions. While this peak is not exclusive to Luminal A, its consistent presence and relative prominence suggest a subtype-associated biochemical characteristic related to carbohydrate and membrane metabolism.

SERS analysis of Luminal A breast cancer samples reveals a reproducible molecular fingerprint characterized by coordinated alterations in proteins, lipids, sugars, and nucleic acids. Sugar-related vibrations in the 422-685 cm^{-1} region highlight altered carbohydrate metabolism, while strong lipid and saccharide contributions between 1064 and 1135 cm^{-1} indicate membrane remodeling. Protein-related bands in the 1172-1297 cm^{-1} range reflect tyrosine residues, peptide bonds, and Amide III vibrations, suggesting modifications in protein secondary structure. Additional lipid-associated features between 1370 and 1462 cm^{-1} confirm fatty acid and cholesterol remodeling. Higher-wavenumber bands at 1537-1557 cm^{-1}, attributed to nucleic acids and aromatic amino acids such as tryptophan, further support involvement of controlled proliferative activity.

Collectively, the Luminal A subtype displays a biochemical landscape characterized by balanced metabolic reprogramming, relatively ordered protein secondary structures, and coordinated lipid and nucleic-acid remodeling, consistent with its less aggressive clinical behavior compared to other breast cancer subtypes.

Table S4 Distribution of SERS shifts in Luminal A (LUMA) Subtype.

SERS shift (cm^{-1})	**LUMA 45**	**LUMA 47**	**LUMA 48**	**LUMA 49**	**LUMA 50**	**LUMA 51**	**LUMA 52**	**LUMA 58**	**Assignment**
422		x	x	x	x	x	x	x	D-(-)-Fructose, citric acid
480				x				x	Saccharides, glycogen
685				x				x	Succinic acid
736		x					x	x	$N^{+}(CH_3)_3$ symmetric stretching of phosphatidylcholine lipids *(choline/phospholipid headgroup region)*
844		x	x	x	x	x		x	C-O-C skeletal mode; monosaccharides; tyrosine; amino acid single-bond stretching
871		x	x		x	x	x		C-C stretching; collagen; lipids; hydroxyproline (collagen I); saccharides, proline
892	**x**	**x**	**x**	**x**	**x**	**x**	**x**	**x**	Protein structural modes (tumor-related)
955				x				x	Lipids; δ(=CH) wagging; C-O stretching of ribose
1006	x							x	Phenylalanine; symmetric ring breathing; collagen
1026					x				C-H in-plane bending mode of phenylalanine
1064	**x**	**x**	**x**	**x**	**x**	**x**	**x**	**x**	Lipid C-C stretch; protein C-O/C-N; O-P-O (DNA/RNA); proline (collagen)
1112	**x**	**x**	**x**	**x**	**x**	**x**	**x**	**x**	C-C stretch (lipid), saccharides
1135	**x**	**x**	**x**	**x**	**x**	**x**	**x**	**x**	C-C skeletal stretching
1172	**x**	**x**	**x**	**x**	**x**	**x**	**x**	**x**	C-H bending of tyrosine
1213				x					Amide III
1254	x				x		x	x	Amide III region (protein secondary structure; can include collagen/lipid contributions)
1276	x		x	x		x			Amide III (α-helix), collagen, lipids
1297	**x**	**x**	**x**	**x**	**x**	**x**	**x**	**x**	Cytosine; ν(CN) and ν(NH); peptide bond (-CONH)
1333				x				x	CH_2 deformation (lipids); adenine/cytosine/tryptophan; α-helix; phospholipids
1370	**x**	**x**	**x**	**x**	**x**	**x**	**x**	**x**	δ(CH_3) symmetric lipid
1418	**x**	**x**	**x**	**x**	**x**	**x**	**x**	**x**	Deoxyribose
1440	**x**	**x**	**x**	**x**	**x**	**x**	**x**	**x**	CH_2 bending (lipids); cholesterol; fatty acids; C-O symmetric stretching
1460		x	x	x	x	x	x	x	Stearic acid

1462	x								Stearic acid
1537			x	x				x	Adenine, guanine, cytosine
1557		x	x			x	x		C=C stretching in tryptophan

Luminal B

Complementing the data for Luminal A, **Table S5** summarizes the distribution of SERS spectral shifts observed in the Luminal B (LUMB) breast cancer subtype. Recurrent peaks were detected at 891, 1064, 1109, 1135, 1172, 1297, 1370, 1418, 1441, and 1461 cm^{-1}. The 891 cm^{-1} band is attributed to protein structural vibrations (49). The 1064 cm^{-1} peak corresponds primarily to C-C stretching in lipids and also includes contributions from C-O and C-N stretching in proteins and phosphate vibrations in nucleic acids (48,49). The 1109 cm^{-1} band is assigned to C-C stretching in lipids and saccharides (49,54,55), while the 1135 cm^{-1} peak corresponds to C-C skeletal vibrations (54). The 1172 cm^{-1} band is associated with C-H bending modes of tyrosine residues (49), and the 1297 cm^{-1} peak is attributed to cytosine and ν(CN) and ν(NH) vibrations of peptide bonds (-CONH) (54,57). Additional lipid-related bands at 1370 cm^{-1}, 1418 cm^{-1}, 1441 cm^{-1}, and 1461 cm^{-1} correspond to symmetric CH_3 deformation, deoxyribose vibrations, CH_2 bending modes in lipids and fatty acids, and stearic acid, respectively (2-3, 6, 10, 13-14, 55, 56).

The presence of the 1172 cm^{-1} tyrosine-related peak in Luminal B, which is also observed in Luminal A and TNBC but absent in the HER2-enriched subtype, suggests a shared protein backbone architecture among these subtypes. This similarity likely reflects conserved aromatic amino acid contributions and protein secondary structures, despite the higher proliferative capacity and distinct signaling pathways associated with Luminal B tumors.

Low-wavenumber peaks in the 417-422 cm^{-1} range indicate alterations in carbohydrate metabolism. Protein-related features between 601 and 933 cm^{-1}, including aromatic amino acid and backbone vibrations, reflect changes in protein structure and organization. Lipid-associated bands spanning 722-1461 cm^{-1}, encompassing phospholipid headgroups and CH_2/CH_3 bending modes, indicate substantial membrane remodeling. Nucleic-acid-associated vibrations in the 1297-1344 cm^{-1} region suggest increased DNA and RNA involvement. Higher-wavenumber bands at 1656-1687 cm^{-1} correspond to Amide I vibrations and lipid C=O stretching, reflecting protein conformational changes and lipid-protein interactions.

Overall, the Luminal B SERS spectra highlight complex molecular alterations involving proteins, lipids, carbohydrates, and nucleic acids, consistent with the increased proliferative activity and intermediate aggressiveness characteristic of this breast cancer subtype.

Table S5 Distribution of SERS shifts in Luminal B (LUMB) Subtype.

SERS shift (cm^{-1})	**LUMB 5**	**LUMB 6**	**LUMB 8**	**LUMB4 5**	**LUMB5 2**	**Assignment**
417	x		x	x		D-(-)-Fructose, citric acid
475				x		Saccharides, glycogen *(carbohydrate region)*
531		x				S-S disulphide bridges in cysteine
601	x			x		Glycerol, tryptophan, phosphatidylinositol
645		x				C-C twisting (tyrosine); C-S stretching
679				x		C-S stretching of cystine / nucleic-acid-linked phospholipids *(~671)* or succinic acid *(~684)*
722	x	x		x		$N^{+}(CH_3)_3$ choline group; phosphatidylcholine/sphingomyelin (membrane headgroup)
748				x		Proteins; symmetric ring breathing of tryptophan
813				x		O-P-O stretch (DNA) / proline-hydroxyproline & lipid CH_2 twisting region
848			x	x		C-O-C skeletal mode; monosaccharides; tyrosine; amino acid stretching
870		x	x			C-C stretching; collagen; lipids; hydroxyproline; saccharides, proline
891	**x**	**x**	**x**	**x**	**x**	Protein structural modes (tumor-related)
933	x	x	x	x		C-C protein backbone (α-helix); collagen; proline/glycogen
1005	x	x	x	x		Phenylalanine; symmetric ring breathing; collagen
1026				x		C-H in-plane bending of phenylalanine
1064	**x**	**x**	**x**	**x**	**x**	Lipid C-C; protein C-O/C-N; O-P-O (DNA/RNA); proline (collagen)
1109	**x**	**x**	**x**	**x**	**x**	C-C stretch (lipid), saccharides
1135	**x**	**x**	**x**	**x**	**x**	C-C skeletal stretching
1172	**x**	**x**	**x**	**x**	**x**	C-H bending of tyrosine
1224			x			Amide III
1234	x	x	x	x		β-sheet / Amide III; CH_2 wagging (glycine, proline)
1244			x		x	Amide III
1297	**x**	**x**	**x**	**x**	**x**	Cytosine; ν(CN) and ν(NH); peptide bond (-CONH)
1336			x	x		CH_2 deformation (lipids); adenine/cytosine/tryptophan; α-helix; phospholipids
1344	x	x				Same region: CH_2 deformation lipid / nucleobase + aromatic contributions
1370	**x**	**x**	**x**	**x**	**x**	$\delta(CH_3)$ symmetric lipid
1418	**x**	**x**	**x**	**x**	**x**	Deoxyribose

1441	**x**	**x**	**x**	**x**	**x**	CH_2 bending (lipids); cholesterol; fatty acids; C-O symmetric stretching
1461	**x**	**x**	**x**	**x**	**x**	Stearic acid
1526				x		Adenine, guanine, cytosine *(nucleobases region)*
1555				x		C=C stretching in tryptophan
1602			x			Aromatic amino acids: phenylalanine/tyrosine/tryptophan (C=C modes)
1601				x		Aromatic amino acids: phenylalanine/tyrosine/tryptophan (C=C modes)
1661		x		x		Amide I (α-helix); C=O stretching; lipid C=C
1687	x					C=O stretching in lipids

To synthesize the findings across all breast cancer subtypes, **Table S6** provides a comprehensive comparison of the major SERS peak positions identified in TNBC, HER2-enriched, Luminal A, and Luminal B tumors, highlighting both shared and subtype-specific molecular signatures.

Overall, SERS spectral analysis reveals that all subtypes share a common set of core vibrational features associated with fundamental cellular components, including protein structural modes (~892-935 cm^{-1}), lipid and membrane-related vibrations (~1064-1135, 1370-1463 cm^{-1}), nucleic-acid-associated bands (~1297-1419 cm^{-1}), and Amide I vibrations (~1656-1687 cm^{-1}). These shared peaks reflect universal hallmarks of malignant transformation such as altered protein conformation, membrane remodeling, and increased nucleic-acid activity. However, clear differences in peak presence, distribution, and clustering distinguish each molecular subtype.

TNBC exhibits the greatest spectral heterogeneity, with prominent low-wavenumber carbohydrate-related peaks (~420-482 cm^{-1}), redox- and metabolism-associated bands (~534, 684 cm^{-1}), and multiple nucleic-acid and aromatic amino acid signals (~707-807, 1531-1599 cm^{-1}), consistent with its aggressive, metabolically flexible phenotype. In contrast, HER2-enriched tumors display a more membrane- and protein-dominated spectral profile, characterized by strong phospholipid choline vibrations (~720-731 cm^{-1}), lipid and protein backbone modes (~1062-1133 cm^{-1}), and pronounced Amide I contributions (~1660-1686 cm^{-1}), reflecting receptor-driven signaling, membrane turnover, and structured protein assemblies.

The Luminal A and Luminal B subtypes share several spectral similarities, particularly tyrosine-associated bands (~1172 cm^{-1}), Amide III vibrations (~1236-1297 cm^{-1}), and lipid remodeling signatures (~1370-1462 cm^{-1}), indicating conserved protein architecture and hormone-related biology. However, Luminal B samples show stronger and more frequent nucleic-acid-related peaks (~1297-1344 cm^{-1}) and enhanced membrane phospholipid signals, suggesting higher proliferative activity and genomic involvement compared with Luminal A. This distinction is clearly visible in the stacked peak overlay, where Luminal B exhibits denser clustering in the lipid and nucleic-acid regions.

Table S6 Summarize of all SERS peaks across all subtypes of breast cancer.

SERS shift (cm^{-1})	TNBC	HER2	LUMA	LUMB
892	x		x	x
1064	x	x	x	x
1112	x		x	x
1135	x	x	x	x
1171		x	x	x
1297	x	x	x	x
1371	x	x	x	x
1419	X	x	x	x
1441	x	x	x	x
1463	x	x		x

Fig. S2 presents the confusion matrix summarizing the performance of the PCA-LDA classifier for breast cancer subtype discrimination using patient-averaged SERS spectra under stratified k-fold cross validation. The matrix illustrates both correctly and incorrectly classified samples across the five tissue classes, highlighting class-specific sensitivity. To further evaluate discriminative performance while accounting for internal validation, receiver operating characteristic (ROC) curves derived from one-vs-rest PCA-LDA models are shown in **Fig. S3**. The corresponding area under the curve (AUC) values indicates moderate to strong subtype-dependent discrimination, with higher AUCs observed for Luminal A and TNBC, and comparatively lower performance for rarer subtypes.

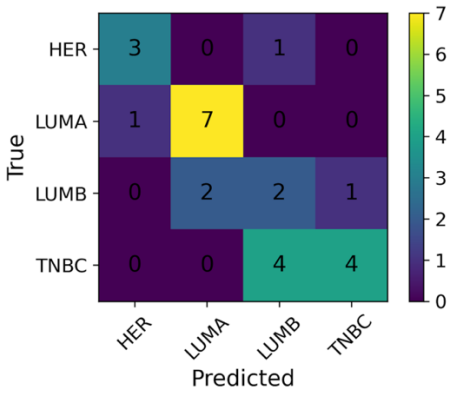

Fig. S2 Confusion matrix for PCA-LDA classification of breast cancer subtypes.

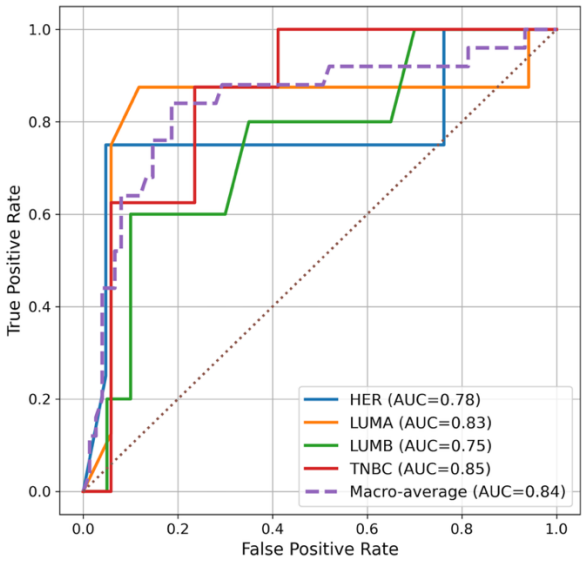

Fig. S 3 Receiver operating characteristic (ROC) curves for PCA-LDA classification.

REFERENCES

1. Kim J, Harper A, McCormack V, Sung H, Houssami N, Morgan E, et al. Global patterns and trends in breast cancer incidence and mortality across 185 countries. Nat Med. 2025 Apr;31(4):1154-62.

2. Moloney BM, O'Loughlin D, Elwahab SA, Kerin MJ. Breast cancer detection—a synopsis of conventional modalities and the potential role of microwave imaging. Diagnostics. 2020;10(2).

3. Nalejska E, Mączyńska E, Lewandowska MA. Prognostic and predictive biomarkers: Tools in personalized oncology. Mol Diagn Ther. 2014;18(3):273-84.

4. Parker JL, Kuzulugil SS, Pereverzev K, Mac S, Lopes G, Shah Z, et al. Does biomarker use in oncology improve clinical trial failure risk? A large-scale analysis. Cancer Med. 2021;10(6):1955-63.

5. Beckman RA, Clark J, Chen C. Integrating predictive biomarkers and classifiers into oncology clinical development programmes. Perspectives (Montclair). 2011;10:735-48.

6. Redonda G. Miller MD. Breast cancer screening can we talk? J Gen Intern Med. 2004;16(3):206-7.

7. Reeves RA, Kaufman T. Mammography. 2023. (National Center for biotechnology Information).

8. Hofvind S, Ponti A, Patnick J, Ascunce N, Njor S, Broeders M, et al. False-Positive Results in Mammographic Screening for Breast Cancer in Europe: A Literature Review and Survey of Service Screening Programmes. J Med Screen. 2012 Sept;19(1_suppl):57-66.

9. Christiansen CL. Predicting the Cumulative Risk of False-Positive Mammograms. J Natl Cancer Inst. 2000 Oct 18;92(20):1657-66.

10. Hubbard RA, Kerlikowske K, Flowers CI, Zhu W, Miglioretti DL. Cumulative probability of false-positive recall or biopsy recommendation after 10 years of screening mammography. 2012;

11. Joy JE, Penhoet EE, Petitti DB. Saving Women's Lives: Strategies for Improving Breast Cancer Detection and Diagnosis [Internet]. Washington, D.C.: National Academies Press; 2005

12. Zahl PH, Mæhlen J, Welch HG. The Natural History of Invasive Breast Cancers Detected by Screening Mammography. Arch Intern Med. 2008 Nov 24;168(21):2311.

13. Løberg M, Lousdal ML, Bretthauer M, Kalager M. Benefits and harms of mammography screening. Breast Cancer Res [Internet]. 2015 May 1;17(1).

14. Puliti D, Duffy SW, Miccinesi G, De Koning H, Lynge E, Zappa M, et al. Overdiagnosis in Mammographic Screening for Breast Cancer in Europe: A Literature Review. J Med Screen. 2012 Sept;19(1_suppl):42-56.

15. Kalager M, Adami HO, Bretthauer M, Tamimi RM. Overdiagnosis of Invasive Breast Cancer Due to Mammography Screening: Results From the Norwegian Screening Program. Ann Intern Med. 2012 Apr 3;156(7):491-9.

16. Boyd NF, Sun L, Stone J, Fishell E, Jong RA, Chiarelli A. Mammographic Density and the Risk and Detection of Breast Cancer. N Engl J Med. 2007;

17. Sickles EA. The Use of Breast Imaging to Screen Women at High Risk for Cancer. Radiol Clin North Am. 2010 Sept;48(5):859-78.

18. Wernli KJ, DeMartini WB, Ichikawa L, Lehman CD, Onega T, Kerlikowske K, et al. Patterns of Breast Magnetic Resonance Imaging Use in Community Practice. JAMA Intern Med. 2014 Jan 1;174(1):125.

19. Berg WA, Blume JD, Adams AM, Jong RA, Barr RG, Lehrer DE, et al. Reasons Women at Elevated Risk of Breast Cancer Refuse Breast MR Imaging Screening: ACRIN 6666. Radiology. 2010 Jan;254(1):79-87.

20. Berg WA, Gutierrez L, NessAiver MS, Carter WB, Bhargavan M, Lewis RS, et al. Diagnostic Accuracy of Mammography, Clinical Examination, US, and MR Imaging in Preoperative Assessment of Breast Cancer. Radiology. 2004 Dec;233(3):830-49.

21. Moisoiu V, Iancu SD, Stefancu A, Moisoiu T, Pardini B, Dragomir MP, et al. SERS liquid biopsy: An emerging tool for medical diagnosis. Colloids Surf B Biointerfaces. 2021;208(August).

22. Li J, Li Y, Li P, Zhang Y, Du L, Wang Y, et al. Exosome detection via surface-enhanced Raman spectroscopy for cancer diagnosis. Acta Biomater. 2022;144:1-14.

23. Li J, Li Y, Li P, Zhang Y, Du L, Wang Y, et al. Exosome detection via surface-enhanced Raman spectroscopy for cancer diagnosis. Acta Biomater. 2022 May;144:1-14.

24. Vendrell M, Maiti KK, Dhaliwal K, Chang YT. Surface-enhanced Raman scattering in cancer detection and imaging. Trends Biotechnol. 2013 Apr;31(4):249-57.

25. Beeram R, Vepa KR, Soma VR. Recent Trends in SERS-Based Plasmonic Sensors for Disease Diagnostics, Biomolecules Detection, and Machine Learning Techniques. Biosensors. 2023 Feb 27;13(3):328.

26. Vázquez-Iglesias L, Stanfoca Casagrande GM, García-Lojo D, Ferro Leal L, Ngo TA, Pérez-Juste J, et al. SERS sensing for cancer biomarker: Approaches and directions. Bioact Mater. 2024 Apr;34:248-68.

27. Xu L, Xie Y, Lin J, Wu A, Jiang T. Advancements in SERS-based biological detection and its application and perspectives in pancreatic cancer. VIEW [Internet]. 2024 Feb;5(1).

28. Lee S, Dang H, Moon JI, Kim K, Joung Y, Park S, et al. SERS-based microdevices for use as *in vitro* diagnostic biosensors. Chem Soc Rev. 2024;53(11):5394-427.

29. Bell SEJ, Charron G, Cortés E, Kneipp J, De La Chapelle ML, Langer J, et al. Towards Reliable and Quantitative Surface-Enhanced Raman Scattering (SERS): From Key Parameters to Good Analytical Practice. Angew Chem Int Ed. 2020 Mar 27;59(14):5454-62.

30. Pérez-Jiménez AI, Lyu D, Lu Z, Liu G, Ren B. Surface-enhanced Raman spectroscopy: benefits, trade-offs and future developments. Chem Sci. 2020;11(18):4563-77.

31. Panneerselvam R, Liu GK, Wang YH, Liu JY, Ding SY, Li JF, et al. Surface-enhanced Raman spectroscopy: bottlenecks and future directions. Chem Commun. 2018;54(1):10-25.

32. Norton RD, Phan HT, Gibbons SN, Haes AJ. Quantitative Surface-Enhanced Spectroscopy. 2022;141-62.

33. Gargiulo J, Berté R, Li Y, Maier SA, Cortés E. From Optical to Chemical Hot Spots in Plasmonics. Acc Chem Res. 2019 Sept 17;52(9):2525-35.

34. Hernandez Cedillo A, Velazquez Salazar JJ, Mendez Lozoya J, Agyei-Mensah JA, Guirado-López RA, Hernandez Cedillo C, et al. Ag@Ni-NiO NW Core-Shell Nanowires: A Reliable Surface-Enhanced Raman Scattering (SERS) Substrate. J Phys Chem C. 2025;

35. Tharwat A, Gaber T, Ibrahim A, Hassanien AE. Linear discriminant analysis: A detailed tutorial. AI Commun. 2017 May 16;30(2):169-90.

36. Dubey SK, Kali M, Hejmady S, Saha RN, Alexander A, Kesharwani P. Recent advances of dendrimers as multifunctional nano-carriers to combat breast cancer. Eur J Pharm Sci. 2021 Sept;164:105890.

37. Prat A, Pineda E, Adamo B, Galván P, Fernández A, Gaba L, et al. Clinical implications of the intrinsic molecular subtypes of breast cancer. The Breast. 2015 Nov;24:S26-35.

38. Nagarajan D, McArdle S. Immune Landscape of Breast Cancers. Biomedicines. 2018 Feb 11;6(1):20.

39. Burguin A, Diorio C, Durocher F. Breast Cancer Treatments: Updates and New Challenges. J Pers Med. 2021 Aug 19;11(8):808.

40. Lee D, Du J, Yu R, Su Y, Heath JR, Wei L. Visualizing Subcellular Enrichment of Glycogen in Live Cancer Cells by Stimulated Raman Scattering. Anal Chem. 2020 Oct 6;92(19):13182-91.

41. Bhattacharjee T, Tawde S, Hudlikar R, Mahimkar M, Maru G, Ingle A, et al. *Ex vivo*Raman spectroscopic study of breast metastatic lesions in lungs in animal models. J Biomed Opt. 2015 Aug 21;20(8):085006.

42. Kast RE, Serhatkulu GK, Cao A, Pandya AK, Dai H, Thakur JS, et al. Raman spectroscopy can differentiate malignant tumors from normal breast tissue and detect early neoplastic changes in a mouse model. Biopolymers. 2008 Mar;89(3):235-41.

43. Fuentes AM, Narayan A, Milligan K, Lum JJ, Brolo AG, Andrews JL, et al. Raman spectroscopy and convolutional neural networks for monitoring biochemical radiation response in breast tumour xenografts. Sci Rep [Internet]. 2023 Jan 27;13(1).

44. Movasaghi Z, Rehman S, Rehman IU. Raman Spectroscopy of Biological Tissues. Appl Spectrosc Rev. 2007 Sept;42(5):493-541.

45. Brożek-Płuska B, Placek I, Kurczewski K, Morawiec Z, Tazbir M, Abramczyk H. Breast cancer diagnostics by Raman spectroscopy. J Mol Liq. 2008 June;141(3):145-8.

46. Zheng C, Liang L, Xu S, Zhang H, Hu C, Bi L, et al. The use of Au@SiO2 shell-isolated nanoparticle-enhanced Raman spectroscopy for human breast cancer detection. Anal Bioanal Chem. 2014 Sept;406(22):5425-32.

47. Haka AS, Shafer-Peltier KE, Fitzmaurice M, Crowe J, Dasari RR, Feld MS. Identifying Microcalcifications in Benign and Malignant Breast Lesions by Probing Differences in Their Chemical Composition Using Raman Spectroscopy.

48. Zúñiga WC, Jones V, Anderson SM, Echevarria A, Miller NL, Stashko C, et al. Raman Spectroscopy for Rapid Evaluation of Surgical Margins during Breast Cancer Lumpectomy. Sci Rep [Internet]. 2019 Oct 10;9(1).

49. Zhang Y, Li Z, Li Z, Wang H, Regmi D, Zhang J, et al. Employing Raman Spectroscopy and Machine Learning for the Identification of Breast Cancer. Biol Proced Online [Internet]. 2024 Sept 12;26(1).

50. Contorno S, Darienzo RE, Tannenbaum R. Evaluation of aromatic amino acids as potential biomarkers in breast cancer by Raman spectroscopy analysis. Sci Rep [Internet]. 2021 Jan 18;11(1).

51. Zheng Q, Li J, Yang L, Zheng B, Wang J, Lv N, et al. Raman spectroscopy as a potential diagnostic tool to analyse biochemical alterations in lung cancer. The Analyst. 2020;145(2):385-92.

52. Abramczyk H, Brozek-Pluska B. Raman Imaging in Biochemical and Biomedical Applications. Diagnosis and Treatment of Breast Cancer. Chem Rev. 2013 Aug 14;113(8):5766-81.

53. Ma M, Zhang J, Liu Y, Wang X, Han B. Advances in the clinical application of Raman spectroscopy in breast cancer. Appl Spectrosc Rev. 2024 Nov 25;59(10):1459-93.

54. Nargis HF, Nawaz H, Bhatti HN, Jilani K, Saleem M. Comparison of surface enhanced Raman spectroscopy and Raman spectroscopy for the detection of breast cancer based on serum samples. Spectrochim Acta A Mol Biomol Spectrosc. 2021 Feb;246:119034.

55. Koya SK, Brusatori M, Yurgelevic S, Huang C, Werner CW, Kast RE, et al. Accurate identification of breast cancer margins in microenvironments of ex-vivo basal and luminal breast cancer tissues using Raman spectroscopy. Prostaglandins Other Lipid Mediat. 2020 Dec;151:106475.

56. De Gelder J, De Gussem K, Vandenabeele P, Moens L. Reference database of Raman spectra of biological molecules. J Raman Spectrosc. 2007 Sept;38(9):1133-47.

57. Lyng FM, Traynor D, Nguyen TNQ, Meade AD, Rakib F, Al-Saady R, et al. Discrimination of breast cancer from benign tumours using Raman spectroscopy. Ahmad A, editor. PLOS ONE. 2019 Feb 14;14(2):e0212376.

58. Toğaçar M, Ergen B, Cömert Z. Application of breast cancer diagnosis based on a combination of convolutional neural networks, ridge regression and linear discriminant analysis using invasive breast cancer images processed with autoencoders. Med Hypotheses. 2020 Feb;135:109503.

59. Wang M, Zhang K, Yue L, Liu X, Lai Y, Zhang H. Robust Diagnosis of Breast Cancer Based on Silver Nanoparticles by Surface-Enhanced Raman Spectroscopy and Machine Learning. ACS Appl Nano Mater. 2024 June 14;7(11):13672-80.

60. Gardner-Lubbe S. Linear discriminant analysis for multiple functional data analysis. J Appl Stat. 2021 Aug 18;48(11):1917-33.

61. Adebiyi MO, Arowolo MO, Mshelia MD, Olugbara OO. A Linear Discriminant Analysis and Classification Model for Breast Cancer Diagnosis. Appl Sci. 2022 Nov 11;12(22):11455.

62. Perou CM, Sørlie T, Eisen MB, Van De Rijn M, Jeffrey SS, Rees CA, et al. Molecular portraits of human breast tumours. Nature. 2000 Aug 17;406(6797):747-52.

63. Yarden Y, Sliwkowski MX. Untangling the ErbB signalling network. Nat Rev Mol Cell Biol. 2001 Feb;2(2):127-37.

64. Iqbal N, Iqbal N. Human Epidermal Growth Factor Receptor 2 (HER2) in Cancers: Overexpression and Therapeutic Implications. Mol Biol Int. 2014 Sept 7;2014:1-9.

65. Melitto AS, Arias VEA, Shida JY, Gebrim LH, Silveira L. Diagnosing molecular subtypes of breast cancer by means of Raman spectroscopy. Lasers Surg Med. 2022 Oct;54(8):1143-56.

66. Githaiga JI, Angeyo HK, Kaduki KA, Bulimo WD, Ojuka DK. Quantitative Raman spectroscopy of breast cancer malignancy utilizing higher-order principal components: A preliminary study. Sci Afr. 2021 Nov;14:e01035.

67. Bitar RA, Martinho HDS, Tierra-Criollo CJ, Zambelli Ramalho LN, Netto MM, Martin AA. Biochemical analysis of human breast tissues using Fourier-transform Raman spectroscopy. J Biomed Opt. 2006;11(5):054001.

68. Li H, Ning T, Yu F, Chen Y, Zhang B, Wang S. Raman Microspectroscopic Investigation and Classification of Breast Cancer Pathological Characteristics. Molecules. 2021 Feb 9;26(4):921.

69. Cao Y, Xiong J, Du Y, Tang Y, Yin L. Raman spectroscopy combined with multivariate statistical algorithms for the simultaneous screening of cervical and breast cancers. Lasers Med Sci [Internet]. 2024 Feb 20;39(1).

70. Kothari R, Fong Y, Storrie-Lombardi MC. Review of Laser Raman Spectroscopy for Surgical Breast Cancer Detection: Stochastic Backpropagation Neural Networks. Sensors. 2020 Nov 2;20(21):6260.

71. Shang L, Tang J, Wu J, Shang H, Huang X, Bao Y, et al. Polarized Micro-Raman Spectroscopy and 2D Convolutional Neural Network Applied to Structural Analysis and Discrimination of Breast Cancer. Biosensors. 2022 Dec 30;13(1):65.

72. Shang LW, Ma DY, Fu JJ, Lu YF, Zhao Y, Xu XY, et al. Fluorescence imaging and Raman spectroscopy applied for the accurate diagnosis of breast cancer with deep learning algorithms. Biomed Opt Express. 2020 July 1;11(7):3673.